

Search for ferromagnetism in Mn-doped lead halide perovskites

Maryam Sajedi^{1,2}, Chen Luo^{1,3}, Konrad Siemensmeyer⁴, Maxim Krivenkov ¹, Kai Chen^{1,5}, James M. Taylor ^{1,3}, Marion A. Flatken⁴, Florin Radu ¹ & Oliver Rader ¹✉

Lead halide perovskites are new key materials in various application areas such as high efficiency photovoltaics, lighting, and photodetectors. Doping with Mn, which is known to enhance the stability, has recently been reported to lead to ferromagnetism below 25 K in methylammonium lead iodide (MAPbI₃) mediated by superexchange. Two most recent reports confirm ferromagnetism up to room temperature but mediated by double exchange between Mn²⁺ and Mn³⁺ ions. Here we investigate a wide concentration range of MAMn_xPb_{1-x}I₃ and Mn-doped triple-cation thin films by soft X-ray absorption, X-ray magnetic circular dichroism, and quantum interference device magnetometry. The X-ray absorption lineshape shows clearly an almost pure Mn²⁺ configuration, confirmed by a sum-rule analysis of the dichroism spectra. A remanent magnetization is not observed down to 2 K. Curie-Weiss fits to the magnetization yield negative Curie temperatures. All data show consistently that significant double exchange and ferromagnetism do not occur. Our results show that Mn is not suitable for creating ferromagnetism in lead halide perovskites.

¹Helmholtz-Zentrum Berlin für Materialien und Energie, Albert-Einstein-Str. 15, 12489 Berlin, Germany. ²Institut für Physik und Astronomie, Universität Potsdam, Karl-Liebknecht-Str. 24/25, 14476 Potsdam, Germany. ³Fakultät für Physik, Technische Universität München, James-Franck-Straße 1, 85748 Garching bei München, Germany. ⁴Helmholtz-Zentrum Berlin für Materialien und Energie, Hahn-Meitner-Platz 1, 14109 Berlin, Germany. ⁵Present address: National Synchrotron Radiation Laboratory, University of Science and Technology of China, Hefei 230029 Anhui, China. ✉email: rader@helmholtz-berlin.de

Lead halide perovskites (LHP) are emergent semiconductors receiving remarkable attention in several research areas thanks to their outstanding transport and optoelectronic properties^{1–3}. Due to the strong spin–orbit coupling acquired by the heavy metal Pb and halogens such as I and Br, LHPs are interesting materials for spintronics. Recently, spin-valve devices have been fabricated based on LHPs interfaced with (La,Sr)MnO₃ and Co⁴. To realize magnetic LHPs, Mn is considered a suitable option as dopant because of its isoelectronic structure to Pb. The incorporation of Mn ions into the lattice structure of LHPs has been proven to improve the crystal quality by limiting the number of generated vacancy defects and reducing carrier recombination⁵. In the doping process, Pb²⁺ can be smoothly replaced by Mn²⁺ thanks to its smaller ionic radius⁵. Recently, the magnetism of Mn-doped MAPbI₃ (where MA is methylammonium CH₃NH₃) was investigated by Náfrádi et al. using electron spin resonance (ESR) and superconducting quantum interference device (SQUID) magnetometry⁶. A plot of the ESR line width versus temperature was interpreted as showing ferromagnetism below 25 K⁶. This was confirmed using SQUID measurements, which also demonstrated a Curie temperature (T_c) of ~25 K⁶. It was suggested that the ferromagnetic ground state is mediated by superexchange which, due to the bond angle of 150°, is not antiferromagnetic. The reported ferromagnetism could be switched off by exposure to visible light⁶. The question of ferromagnetism in Mn-doped MAPbI₃ was raised again by Ren et al.⁷. From SQUID hysteresis loops, it was found that the system is ferromagnetic even at room temperature. This is a very interesting finding since room temperature ferromagnetism has been predicted in Mn-doped wide-band-gap semiconductors, but the highest measured Curie temperature has so far been ~190 K for Mn-doped GaAs fulfilling the theoretical predictions for that system^{8,9}. In the work by Ren et al.⁷, the double exchange of Mn²⁺ and Mn³⁺ via iodine was proposed as the origin of the ferromagnetism⁷. This conclusion was supported by Mn 2*p* core level photoemission spectra from which a stoichiometric ratio of Mn²⁺:Mn³⁺ of ~3:1 was derived⁷. It was also found that an external magnetic field of 1 T increases the photocurrent by 0.5%⁷. Finally, a third study of the magnetic properties of Mn-doped MAPbI₃ by Rajamanickam et al.¹⁰ found very pronounced hysteresis curves with a coercivity of ~0.5 T at room temperature for 15% Mn-doped MAPbI₃. Rajamanickam et al. investigated the origin of room-temperature ferromagnetism as well. They also employed Mn 2*p* core-level fitting and obtained a ratio of Mn²⁺:Mn³⁺ of ~14:1 for a Mn concentration of 5% and ~18:1 for

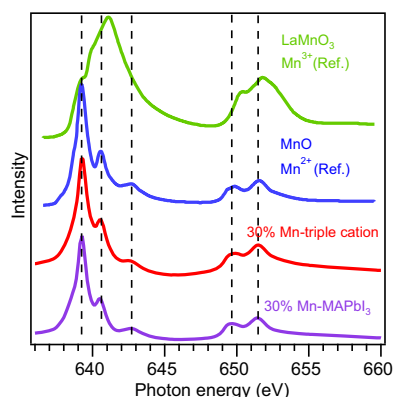


Fig. 1 Identification of Mn valence states using X-ray absorption spectroscopy (XAS). Mn $L_{2,3}$ XAS spectra measured in total electron yield mode of a $\text{MAMn}_{0.03}\text{Pb}_{0.71}\text{I}_3$ and triple-cation film with 30% Mn-doping in comparison with the reference spectra for Mn²⁺ from MnO and Mn³⁺ from LaMnO₃ by Vasiliev et al. (shifted by 1.44 eV)¹³.

the sample with 15% Mn. Based on this result, the authors confirmed double exchange as the origin of the ferromagnetism¹⁰. We have recently begun to investigate the origin of the high efficiency of LHPs by synchrotron radiation methods which have seldom been employed in this material class. In this way, it was revealed that a giant Rashba effect in the valence band suggested as the origin of the long carrier lifetimes does not exist¹¹. We also showed that large polaron formation could not be concluded from photoemission data¹². In the present work, we employ a combination of soft X-ray absorption spectroscopy (XAS), soft X-ray magnetic circular dichroism (XMCD), and SQUID magnetometry, which are essential tools to clarify the question of ferromagnetism in dilute systems and its origin. We apply XMCD sum rules to explore the spin and orbital magnetic moments of Mn. Through detailed temperature-dependent magnetization experiments, we scrutinize the magnetic properties of a series of high-quality monocrystals and thin films of Mn-doped MAPbI₃ as well as mixed triple-cation $\text{Cs}_{0.05}\text{MA}_{0.14}\text{FA}_{0.81}\text{Mn}_x\text{Pb}_{1-x}(\text{I}_{0.85}\text{Br}_{0.15})_3$ thin films (FA denotes formamidinium HC(NH₂)₂). For brevity, the latter structure will be referred to as triple-cation films in what follows. It is worth noting that we have doped perovskites by adding a bivalent salt Mn(II)I₂. This is to preserve the Mn²⁺ ions from possible oxidations by preventing them from involving in any redox exchange reaction. We use Brillouin-function fits to determine the magnetic moment. We conclude that the systems are not ferromagnetic down to at least 2 K and that there is no spectroscopic support for double exchange.

Results and discussion

To clarify the magnetization and valence states of Mn-doped LHPs, we examined several halide perovskites, namely a 3% Mn-doped MAPbI₃ ($\text{MAMn}_{0.03}\text{Pb}_{0.97}\text{I}_3$) single crystal (of size $4 \times 4 \times 1 \text{ mm}^3$), polycrystalline films of $\text{MAMn}_x\text{Pb}_{1-x}\text{I}_3$ with $x = 0.1$ and 0.3 , and triple-cation films with stoichiometric Mn doping contents of 0.1 and 0.3 using the XAS technique. In order to identify the line shape of our XAS spectra and discern the presence of Mn²⁺ and Mn³⁺ ions in the system, in Fig. 1, we compare the XAS $L_{2,3}$ absorption edges from two of the examined systems to MnO Mn²⁺ and LaMnO₃ Mn³⁺ reference spectra from the literature¹³. The XAS spectra of Mn-doped LHPs shown in Fig. 1 are representative of all Mn concentrations studied in the present work. From the comparison of the spectra, it is immediately apparent that Mn is in a 2+ valence state and that there is no Mn³⁺ component. We can safely conclude that the ratio Mn²⁺:Mn³⁺ is larger than 50:1 (see also Fig. S3 and Supplementary Note 2). This is rather similar to Mn-doped GaAs, where Mn also demonstrates a valence state of Mn²⁺^{14–16}. Because Mn³⁺ is required for the double exchange scenario, we conclude that the conditions for double exchange are not present in Mn-doped lead halide perovskites; thus, it cannot be the cause of ferromagnetism neither at low temperature nor at room temperature. Beyond the overall features that distinguish Mn²⁺ from Mn³⁺, a subtle difference is expected between octahedral and tetrahedral Mn²⁺^{17,18}. Since both lineshapes seem to occur in MnO^{13,18} where Mn is octahedral, it appears too early to conclude on the geometry of Mn in the present sample. It might be that the spectral shape indicates interstitial Mn. For Mn in GaAs, it was possible to distinguish interstitial and substitutional Mn from their field-dependent XMCD lineshape¹⁶. The question of substitutional or interstitial Mn in LHPs is highly debated, but at least in 2D perovskites, there are indications from strain analysis and density functional theory that interstitial Mn is present¹⁹. We also note that we do not find any indication of structural degradation with synchrotron light.

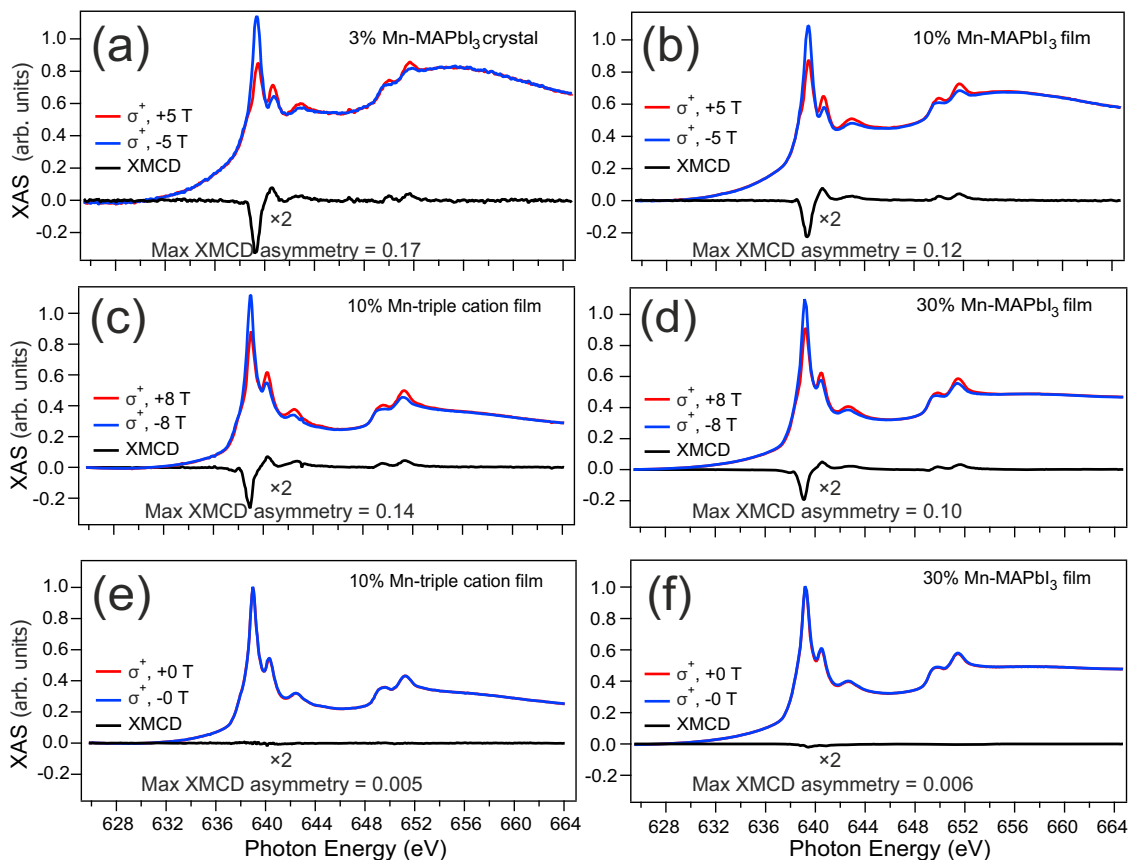


Fig. 2 Low-temperature (8.5 K) Mn $L_{2,3}$ X-ray absorption spectroscopy (XAS) and corresponding X-ray magnetic circular dichroism (XMCD) spectra in total electron yield. **a** $\text{MAMn}_{0.03}\text{Pb}_{0.97}\text{I}_3$ single crystal, **b** $\text{MAMn}_{0.1}\text{Pb}_{0.9}\text{I}_3$ film, **c** triple-cation film with 10% Mn, and **d** $\text{MAMn}_{0.3}\text{Pb}_{0.7}\text{I}_3$ film. Measurements of **a** and **b** are performed under a magnetic field of ± 5 T, while **c** and **d** are measured under ± 8 T. **e**, **f** Represent the XAS/XMCD spectra under the field of ± 0 T after magnetization at 8 T for triple-cation with 10% Mn and $\text{MAMn}_{0.3}\text{Pb}_{0.9}\text{I}_3$ films, respectively. The magnetic field is applied **a**, **b** perpendicular, and **c-f** parallel to the surface.

Figure 2 shows the normalized Mn $L_{2,3}$ absorption edge spectra for right-handed circularly polarized light (σ^+) at magnetic fields of 0, 5, and 8 T and at cryogenic temperature ($T = 8.5$ K). The photon energies of the Mn L_3 and L_2 edges, which have been used to measure magnetic hysteresis loops, are 639 and 651 eV, respectively. The differences between the XAS spectra measured with positive (red) and negative (blue) magnetic fields, i.e., XMCD spectra (black lines) at both the L_3 and L_2 edges, indicates strong magnetization of Mn local moments and large spin polarization of Mn d^5 states at 5 and 8 T [Fig. 2a–d]. The XMCD signal clearly changes sign between the low-energy L_3 and high-energy L_2 edges, as expected. Among the systems studied, the monocrystal of $\text{MAMn}_{0.03}\text{Pb}_{0.97}\text{I}_3$ demonstrates the largest XMCD asymmetry $(I(\sigma^+) - I(\sigma^-))/(I(\sigma^+) + I(\sigma^-))$ of 0.17 at 8.5 K.

The other systems, which are in the form of polycrystalline thin films, also demonstrate spatially homogeneous XAS and XMCD line shapes that are consistent between 10% and 30% Mn content. We find that the Mn-doped MAPbI_3 and triple-cation films show similar magnetic properties. This indicates that the Mn ions are homogeneously distributed throughout the polycrystalline films. Furthermore, in order to search for long-range ferromagnetic order, the samples were magnetized in the surface plane at 8.5 K via a field of 8 T, and then the XAS spectra were taken in zero field. Figure 2e, f shows the resulting XAS spectra measured at remanence. The XMCD difference is nearly zero. This lack of remanent magnetization demonstrates the absence of ferromagnetism in these systems. See also Fig. S4 and Supplementary

Note 3 for XAS spectra measured in remanence as well as XAS spectra taken at room temperature of the other samples.

The spin and orbital magnetic moments of Mn in the $\text{MAMn}_{0.3}\text{Pb}_{0.7}\text{I}_3$ system are determined by applying the XMCD sum rule analysis²⁰ and shown in Fig. 3a, b. The number of unpaired holes of Mn 3d is considered as $n_h = 4.52$, according to similar analyses with Mn^{2+} -doped systems^{21–23}. The degree of light polarization in the experiment is $p = 0.77$, and a correction factor for the spin magnetic moment of 1.47 is used, which is found in similar cases for Mn^{2+} ^{24–26}. Corrections with the light polarization factor p have not been employed to the data as displayed in Figs. 2 and 3. Prior to the integration of the XAS spectra of $\text{MAMn}_{0.3}\text{Pb}_{0.7}\text{I}_3$ shown in Fig. 3a, a background signal was subtracted. The background spectra were obtained from a reference sample without any Mn dopant. For the $\text{MAMn}_{0.3}\text{Pb}_{0.7}\text{I}_3$ film, we obtain an ordered spin magnetic moment per atom of $m_{z,\text{spin}} = 0.934 \mu_B$, orbital moment of $m_{z,\text{orbit}} = 0.017 \mu_B$, and a total experimental magnetic moment of $m_z = m_{z,\text{spin}} + m_{z,\text{orbit}} = 0.951 \mu_B$ [see Fig. 2d]. As expected for Mn^{2+} , the orbital moment is negligible, and hence the Landé factor $g_j = 2.0$.

To investigate the possibility of ferromagnetism further, full hysteresis curves have been measured. The upper row in Fig. 4 shows the magnetic field dependence $M(H)$ of data extracted from the XMCD signal. These data have the advantage that they probe the magnetism of Mn directly, unlike the case with SQUID. Moreover, this method does not require the subtraction of paramagnetic contributions from the substrate of the film. The XMCD field dependence yields $M(H)$ loops measured at 639 eV

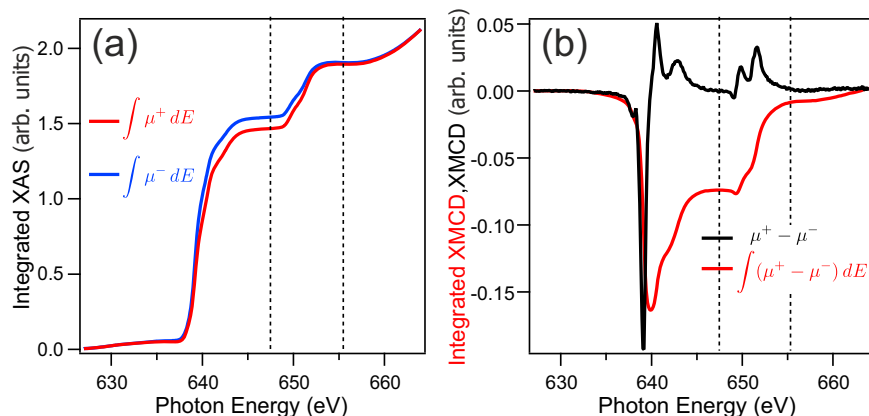


Fig. 3 X-ray magnetic circular dichroism (XMCD) sum rule calculated for $\text{MAMn}_{0.03}\text{Pb}_{0.97}\text{I}_3$. **a** Integration of X-ray absorption spectroscopy (XAS) $L_{2,3}$ edges for ± 8 T, at 8.5 K. **b** XMCD and its corresponding integration. The magnetic field is parallel to the surface plane.

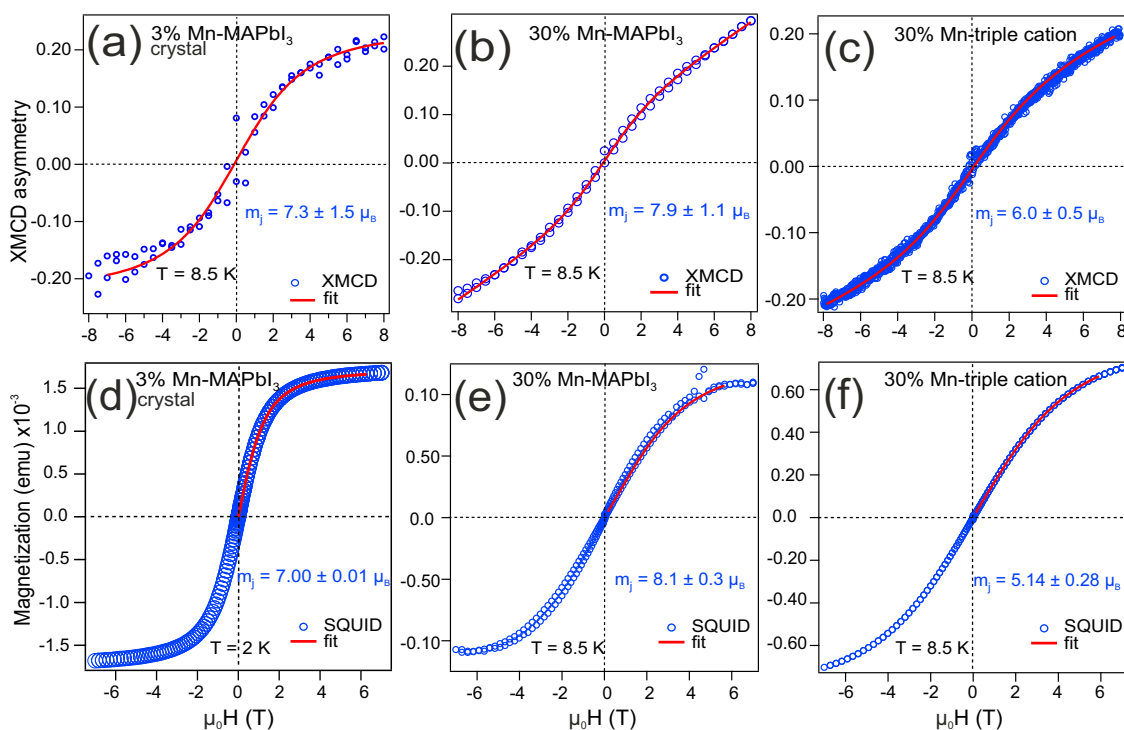


Fig. 4 Magnetic-field (H) dependence of the X-ray magnetic circular dichroism (XMCD) asymmetry at the Mn L_3 -edge and magnetization $M(H)$ using superconducting quantum interference device (SQUID). **a–c** H dependence with the field applied perpendicular to the surface at 8.5 K for **a** $\text{MAMn}_{0.03}\text{Pb}_{0.97}\text{I}_3$ crystal, **b** Mn-doped MAPbI_3 , and **c** triple-cation films. $M(H)$ was measured with SQUID for **d** $\text{MAMn}_{0.03}\text{Pb}_{0.97}\text{I}_3$ crystal at 2 K, and **e, f** for Mn-doped MAPbI_3 and triple-cation films at 8.5 K, respectively. The magnetic field applied in SQUID is parallel to the sample plane. Red solid lines represent the fits of the Brillouin function to the data.

(L_3 -edge), with the magnetic field sweeping from -8 to $+8$ T at 8.5 K [Fig. 4a–c]. We observe no remanence or coercivity, which provides further evidence for the lack of ferromagnetic order in the single crystal and the different thin film samples studied. We verified this response to the external magnetic field by measuring SQUID magnetometry up to ± 6 T in the $\text{MAMn}_{0.03}\text{Pb}_{0.97}\text{I}_3$ single crystal at 2 K [Fig. 4d] and in the Mn-doped MAPbI_3 and triple-cation thin films at 8.5 K [Fig. 4e, f]. A fair match is observed between low-temperature $M(H)$ data from XMCD and SQUID measurements. Both data sets reveal a hyperbolic tangent or S-like shape. Note that the XMCD in Fig. 4 has been measured with the magnetic field and XMCD detection perpendicular to the surface plane, while SQUID has been measured for an in-plane magnetic field. Their similarity indicates the absence of

substantial magnetic anisotropy. In order to quantify the S-shape of the $M(H)$ data, we fitted these data with a Brillouin function (solid lines in Fig. 4). In addition, to have a broader basis for the Brillouin-function modelling, we have also obtained temperature-dependent data both by XMCD and by SQUID, which are shown in Fig. 5a–f. From the SQUID data, we performed Curie-Weiss fits and obtained negative Curie temperatures θ_C , which indicate antiferromagnetic interactions between the moments as an effect of neighbouring spins. Insets in Fig. 5d, f represent the Curie-Weiss fits on their temperature-dependent inverse magnetization from the SQUID signal after diamagnetic parts have been subtracted. The Curie-Weiss temperatures are in the range of -14.5 to -3.30 K and are shown in Table 1. This result further supports the absence of ferromagnetism.

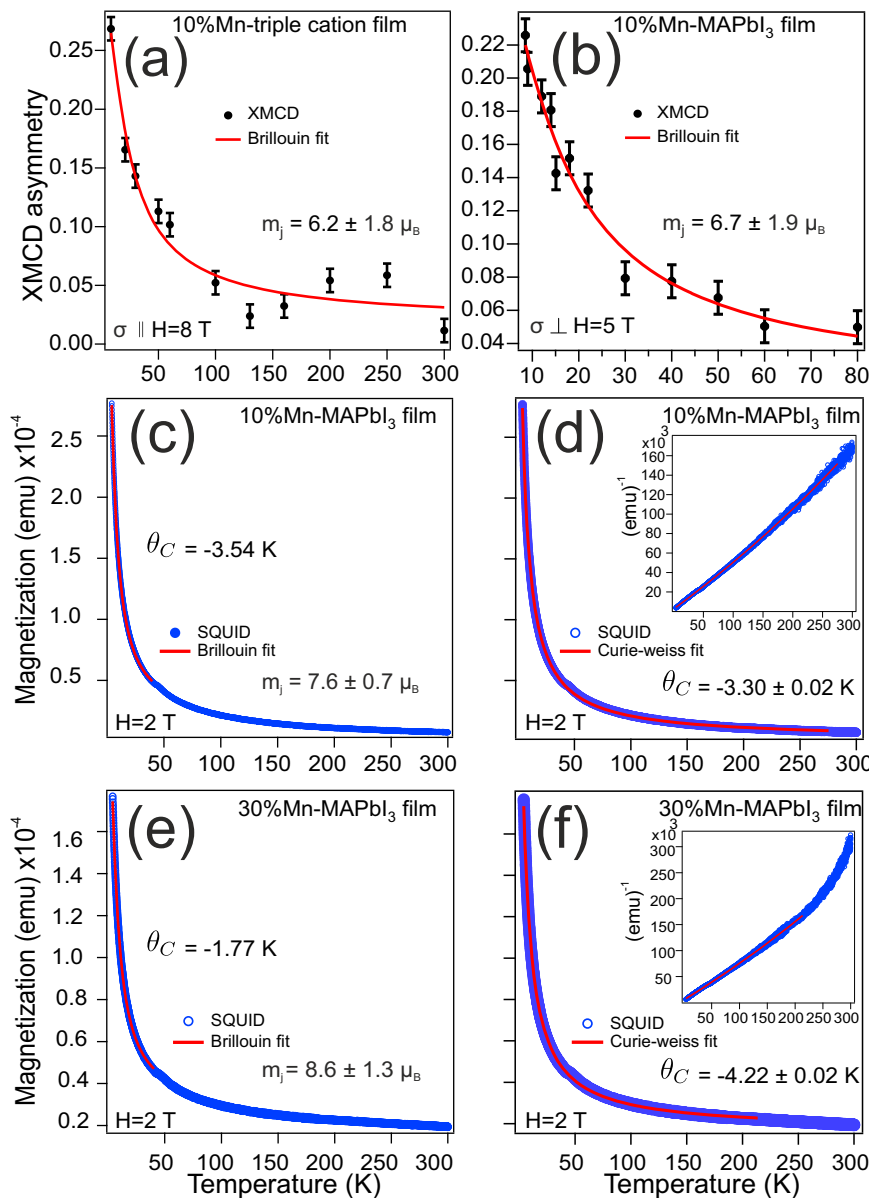


Fig. 5 Temperature evolution of X-ray magnetic circular dichroism (XMCD) asymmetry peak intensity from the Mn L_3 edge and magnetization from superconducting quantum interference device (SQUID). Temperature dependence of XMCD under the field of 8 T for **a** parallel and **b** perpendicular to the surface, along with their Brillouin function fits (solid red lines). **c–f** Magnetization from SQUID of films plotted as a function of temperature while heating recorded under an applied field of 2 T parallel to the surface. Temperature-dependent components have been fitted by both modified Brillouin (**c**, **e**) and the Curie–Weiss functions (**d**, **f**). Solid red lines in the insets of (**d**, **f**) represent the Curie–Weiss fit the inverse magnetization in the low-temperature regime, where the diamagnetic portion of the signal has been subtracted prior to the fits.

The results in terms of paramagnetic moments from the field-dependent measurements of Fig. 4 are referred to in Table 2. We see that the magnetic moments are much larger ($5.14\text{--}8.1 \mu_B$) than those obtained from the sum rule analysis ($0.95 \mu_B$). There are two aspects to discuss here. Firstly, the sum-rule analysis was performed far from magnetic saturation, and the resulting magnetic moment of $0.95 \mu_B$ per Mn ion is therefore underestimated. Secondly, there may be local polarization effects and/or local coupling between Mn moments, which would lead to a total moment above the maximum $3d$ atomic moment of $5 \mu_B$. We have also applied the Brillouin function to fit the temperature-dependent SQUID data in Fig. 5. Here, the fit results depend on the temperature range. We note that the exchange interactions between neighboring spins have been taken into account in the modified Brillouin fit function (effective field is introduced as

described in the literature²⁷) applied to the SQUID data in Fig. 4d–f and Fig. 5c, e. The consideration of this interaction based on the results of the Curie–Weiss fits does not have a significant impact on the resulting magnetic moments. Therefore, for the XMCD results (with larger error bars), we applied Brillouin functions without the inclusion of interactions. We remark that the Curie–Weiss law only holds as an adequate high-temperature approximation for the temperature dependence of magnetization in the absence of strong spin–orbit coupling²⁸. For the fitting analysis with a Brillouin function, on the other hand, it is very challenging to subtract the diamagnetic part at high temperatures, where the magnetic signal drops significantly. Therefore, we limited the fitting range to the low-temperature region in temperature-dependent SQUID results for the approximations with the Brillouin function. The fitting range is

Table 1 Curie-Weiss temperatures (in K) extracted from temperature-dependent data fitted with the Curie-Weiss function.

	10% Mn-MAPbI ₃ film	30% Mn-MAPbI ₃ film	10% Mn-triple-cation film
XMCD	-8.4 ± 3.3 (\perp)	-	-14.5 ± 3.4 (\parallel)
SQUID	-3.30 ± 0.02 (\parallel)	-4.22 ± 0.02 (\parallel)	-

Signs \perp (\parallel) refer to the magnetic field applied perpendicular (parallel) to the sample plane.

Table 2 Overview of magnetic moment values in μ_B extracted from field-dependent measurements (Fig. 4).

	3% Mn-MAPbI ₃ crystal	30% Mn-MAPbI ₃ film	30% Mn-triple-cation film
XMCD (\perp)	7.3 ± 1.5	7.9 ± 1.1	6.0 ± 0.5
SQUID (\parallel)	7.00 ± 0.01	8.1 ± 0.3	5.14 ± 0.28

The signs \perp and \parallel denote magnetic field perpendicular and parallel to the surface plane, respectively.

thus limited to temperatures ≤ 50 K, which have a smaller fitting error [see Fig. 5c, e]. For the determination of magnetic moment, we can compare the values shown in Table 3, ranging from 6.2 to 8.6 μ_B , with those in Table 2 (5.14–8.1 μ_B). A specific dependence on the Mn concentration is not observed.

We compare our current findings with previously published results. Náfrádi et al.⁶ suggested that ferromagnetic superexchange overcomes the usually antiferromagnetic superexchange between Mn moments because the bond angle deviates from 180°. The negative Θ_C values that we obtain indicate instead that antiferromagnetic coupling prevails. Double exchange, as has been proposed recently^{7,10}, requires magnetic ions in two different charge states. This is realized, for example, in manganites²⁹ and involves electron hopping between d states at or near the Fermi level. The strongest coupling and highest T_c occur when the involved ions, here Mn²⁺ and Mn³⁺, have equal concentration⁹.

In the previous studies of Mn-doped MAPbI₃, Mn 2*p* core-level photoelectron spectra have been fitted to determine the ratio of Mn²⁺ to Mn³⁺ components^{7,10}. The spectra are, however, strongly overlapping with intense Pb 4*p* signal from the host material^{7,10}. Ren et al.⁷ show a spin-orbit splitting of Pb 4*p* of 8 eV in their XPS fits (Fig. 4c in Ren et al.⁷). The Pb 4*p* doublet, however, has an established value of spin-orbit splitting of 118 eV³⁰. For Mn²⁺ 2*p*, they used a spin-orbit splitting of 6 eV instead of the established value of 11 eV³⁰, and the Mn³⁺ 2*p*_{1/2} peak is missing in their fit completely. The Mn³⁺ to Mn²⁺ ratios of 14:1 and 18:1 in Rajamanickam et al.¹⁰ are obtained from a similar analysis of XPS spectra, including the incorrect spin-orbit splitting of Pb 4*p*. Note that in Fig. 5 of Rajamanickam et al., the analysis has to be revised as splittings, intensity ratios, and line widths are incorrect. Therefore, the derivation of the Mn²⁺ to Mn³⁺ ratio in these two papers lacks any validity. In general, the Mn *L*-edge XAS spectra that we use are much more sensitive to the different Mn than Mn 2*p* XPS. Moreover, there is no overlapping signal from the Pb due to the lack of unoccupied Pb *d* states near the Fermi energy. Accordingly, by subtraction of the reference spectra and comparison with artificial spectra with different ratios of Mn²⁺ and Mn³⁺ components, we can estimate an upper limit for the amount of Mn³⁺ as 2% of the total Mn amount. Also, for Mn in GaAs, a similarly pure Mn²⁺ line-shape³¹ has been measured. This is, however, due to a

Table 3 Magnetic moment in μ_B values extracted from temperature-dependent measurements (Fig. 5), fitted with Brillouin function.

	10% Mn-MAPbI ₃ film	30% Mn-MAPbI ₃ film	10% Mn-triple-cation film
XMCD (\parallel)	6.7 ± 1.9	-	6.2 ± 1.8
SQUID (\parallel)	7.6 ± 0.7	8.6 ± 1.3	-

paramagnetic Mn component, whereas the ferromagnetic Mn deviates from the pure Mn²⁺ line shape¹⁶.

In the case of SQUID data measured by Náfrádi et al.⁶, the measured spontaneous magnetization reaches only 1.2×10^{-7} emu. This order of magnitude is near the detection limit of SQUID, and it is known that spurious hysteresis signals on the 10^{-7} emu level can frequently appear, as discussed previously^{32–34}. The measured sample with 10% Mn-doping consisted of crystallites of 5–20 nm in length and 0.1 mm diameter⁶. For ESR, 10–15 crystallites were assembled together⁶. Accordingly, we estimated the number of Mn ions to be $(2–8) \times 10^{20}$ and the magnetization per ion to be between $(2–6) \times 10^{-8} \mu_B$ for 10 crystallites. We obtain in our experiments three orders of magnitude larger signal from about four orders of magnitude smaller sample volume. Therefore, several orders of magnitude larger signals are expected, and consequently, we suggest the signal attributed to ferromagnetism by Náfrádi et al.⁶ is too small to be due to the Mn in the sample. Ren et al.⁷ reported a very small hysteresis with non-saturating magnetization and apparent coercivity < 100 Oe. In contrast, the hysteresis in Rajamanickam et al.¹⁰ is very pronounced at room temperature. However, the saturation magnetization is high only for 15% Mn and almost disappears for 10% and 20% Mn¹⁰. Moreover, the strong hysteresis shown at room temperature is inconsistent with the magnetization, which disappears above 170 K in the same work¹⁰. On the other hand, the SQUID results in the present work have instead been obtained for a large Mn concentration range, been verified by XMCD, conducted as a function of magnetic field and temperature, and are therefore more reliable than those in the previous studies^{6,7,10}.

Conclusions

In conclusion, we have conducted XAS, XMCD, and SQUID measurements to investigate the electronic configuration and magnetism in various Mn-doped halide perovskites in the forms of monocrystalline MAPbI₃ and polycrystalline MAPbI₃ as well as triple-cation thin films. We conclude that previous reports that Mn incorporation induces ferromagnetism in MAPbI₃ perovskites are not confirmed within this study. It is also important to note that the preparation conditions here and in the previous papers do not give rise to the expectation that principle differences should occur between samples. Our study calls into question the validity of all 3 previous papers regarding both ferromagnetism and the presence of Mn³⁺. We emphasize the importance of evaluating the magnetic properties by means of element-specific techniques like XAS and XMCD. The XAS data exclude the presence of a significant amount of Mn³⁺, which would be required for a double exchange. Instead of ferromagnetic behavior, paramagnetism was observed.

Experimental methods

The MAPbI₃ single crystal was grown with a solution-based technique called inverse temperature crystallization, as described previously^{35,36}. Mn incorporation was achieved by implementation of manganese (II) iodide powder (MnI₂, 99.9% from Sigma-Aldrich) inside the perovskite solution dissolved in a low

solubility solvent such as γ -butyrolactone at 120 °C. Crystals in black color are grown up to dimensions of $4 \times 4 \times 1 \text{ mm}^3$. To prevent unwanted oxidation and reaction with moisture, the synthesized crystals were immediately transferred and kept in an Ar glovebox prior to the measurements. The crystals were cleaved in situ inside an ultra-high vacuum chamber prior to the experiments by hitting a top post glued onto the surface with a wobble stick at a pressure lower than 1×10^{-10} mbar.

For the precursor preparation of $\text{MAMn}_x\text{Pb}_{1-x}\text{I}_3$ thin film perovskite, the dispersion is mixed from PbI_2 (Tokyo Chemical Industry, purity > 98%) and $\text{CH}_3\text{NH}_3\text{I}$ (Dyename, purity > 99.99%) 1:1 in a mixed solvent with *N,N*-dimethylformamide (DMF) and dimethyl sulfoxide from Sigma-Aldrich prepared by volume ratio of 6:1 reaching a concentration of 1 mole per liter). Preparation of triple-cation perovskite film composition of $\text{Cs}_{0.05}\text{MA}_{0.14}\text{FA}_{0.81}\text{Mn}_x\text{Pb}_{1-x}(\text{I}_{0.85}\text{Br}_{0.15})_3$ with and without Mn is mainly adopted from Saliba et al.³⁷ For the implementation of MnI_2 in the films the respective powder is dissolved in DMF (1 mole per liter) and added to the MAPbI_3 as well as to the triple-cation perovskite precursor dispersion with a relative content of 10% and 30% volume. All chemicals used were of analytical grade and were used as received without any further purification. $\text{MAMn}_x\text{Pb}_{1-x}\text{I}_3$ and triple-cation films of typically 350–450 nm thickness were deposited on Cu and Mo substrates by a spin-coating technique at the rate of 3000 rpm, followed by annealing at 120 °C for 15 min. In order to protect the films from oxidation, a capping layer of about 3 nm C_{60} was deposited on top via chemical vapor deposition, and samples were kept in an Ar box prior to the measurements. The composition and the lattice parameters were verified with energy-dispersive X-ray spectroscopy (EDX), scanning electron microscopy (SEM), and X-ray diffraction (XRD) patterns (see Figs. S1, S2 and Supplementary Note 1). XRD spectra are obtained using Bruker D8 crystallography X-ray tubes at the CoreLab lab facility of Helmholtz-Zentrum Berlin. Soft-X-ray absorption spectra were observed by measuring the total-electron yield. The XAS and XMCD measurements were performed at temperatures ranging from 8.5 to 300 K in the VEKMAG endstation³⁸ at the dipole beamline PM2 of the BESSY II radiation source, reversing the magnetic field from -8 to $+8$ T between complete photon energy scans for each helicity of the circularly polarized dipole radiation. The magnetic field was applied parallel to the synchrotron radiation beam. The degree of circular light polarization was $p = 0.77$, for which the data in Figs. 1, 2, 4, and 5 have not been corrected, i.e., raw data are shown. A commercial SQUID (Quantum Design MPMS XL) was used with a magnetic field of up to 7 T for further magnetic investigations.

Data availability

Data are available from the authors upon reasonable request.

Received: 31 July 2022; Accepted: 17 March 2023;

Published online: 21 April 2023

References

- Ahmad, S., Kazim, S. & Grätzel, M. *Perovskite Solar Cells: Materials, Processes, and Devices* (Wiley-VCH, Weinheim, 2022).
- Park, N.-G. & Segawa, H. *Multifunctional Organic-Inorganic Halide Perovskite: Applications in Solar Cells, Light-Emitting Diodes, and Resistive Memory* (Taylor & Francis, New York, 2022).
- Stoumpos, C. C. & Kanatzidis, M. G. The renaissance of halide perovskites and their evolution as emerging semiconductors. *Acc. Chem. Res.* **48**, 2791–2802 (2015).
- Wang, J. et al. Tunable spin characteristic properties in spin valve devices based on hybrid organic-inorganic perovskites. *Adv. Mater.* **31**, 1904059 (2019).
- Liu, W. et al. Efficient perovskite solar cells fabricated by manganese cations incorporated in hybrid perovskites. *J. Mater. Chem. C* **7**, 11943–11952 (2019).
- Náfrádi, B. et al. Optically switched magnetism in photovoltaic perovskite $\text{CH}_3\text{NH}_3(\text{Mn:Pb})\text{I}_3$. *Nat. Commun.* **7**, 13406 (2016).
- Ren, L. et al. Tuning magnetism and photocurrent in Mn-doped organic-inorganic perovskites. *J. Phys. Chem. Lett.* **11**, 2577–2584 (2020).
- Dietl, T., Ohno, H., Matsukura, F., Cibert, J. & Ferrand, D. Zener model description of ferromagnetism in zinc-blende magnetic semiconductors. *Science* **287**, 1019–1022 (2000).
- Dietl, T. & Ohno, H. Dilute ferromagnetic semiconductors: physics and spintronic structures. *Rev. Mod. Phys.* **86**, 187 (2014).
- Rajamanickam, N., Chowdhury, T. H., Isogami, S. & Islam, A. Magnetic properties in CH_3NH_3 perovskite thin films by Mn doping. *J. Phys. Chem. C* **125**, 20104–20112 (2021).
- Sajedi, M. et al. Absence of a giant Rashba effect in the valence band of lead halide perovskites. *Phys. Rev. B* **102**, 081116(R) (2020).
- Sajedi, M. et al. Is there a Polaron signature in angle-resolved photoemission of CsPbBr_3 ? *Phys. Rev. Lett.* **128**, 176405 (2022).
- Vasiliev, A. N. et al. Valence states and metamagnetic phase transition in partially B-site-disordered perovskite $\text{EuMn}_{0.5}\text{Co}_{0.5}\text{O}_3$. *Phys. Rev. B* **77**, 104442 (2008).
- Ohldag, H. et al. Magnetic moment of Mn in the ferromagnetic semiconductor $(\text{Ga}_{0.98}\text{Mn}_{0.02})\text{As}$. *Appl. Phys. Lett.* **76**, 2928–2930 (2000).
- Ueda, S. et al. Magnetic circular dichroism in Mn 2p core absorption of $\text{Ga}_{1-x}\text{Mn}_x\text{As}$. *Physica E* **10**, 210–214 (2001).
- Rader, O. et al. Identification of extrinsic Mn contributions in $\text{Ga}_{1-x}\text{Mn}_x\text{As}$ by field-dependent magnetic circular X-ray dichroism. *J. Electron Spectrosc. Relat. Phenom.* **144**, 789–792 (2005).
- Kubin, M. et al. Probing the oxidation state of transition metal complexes: a case study on how charge and spin densities determine Mn L-edge X-ray absorption energies. *Chem. Sci.* **9**, 6813–6829 (2018).
- Nemrava, S. et al. Three oxidation states of manganese in the barium hexaferrite $\text{BaFe}_{12-x}\text{Mn}_x\text{O}_{19}$. *Inorg. Chem.* **56**, 3861–3866 (2017).
- Torma, A. J. et al. Interstitial nature of Mn^{2+} doping in 2D perovskites. *ACS Nano* **15**, 20550–20561 (2021).
- Chen, C. et al. Experimental confirmation of the X-ray magnetic circular dichroism sum rules for iron and cobalt. *Phys. Rev. Lett.* **75**, 152 (1995).
- Galanakis, I., Dederichs, P. & Papanikolaou, N. Slater-Pauling behavior and origin of the half-metallicity of the full-Heusler alloys. *Phys. Rev. B* **66**, 174429 (2002).
- Schmalhorst, J. et al. Interface structure and magnetism of magnetic tunnel junctions with a Co_2MnSi electrode. *Phys. Rev. B* **70**, 024426 (2004).
- Goering, E. X-ray magnetic circular dichroism sum rule correction for the light transition metals. *Philos. Mag. Lett.* **85**, 2895–2911 (2005).
- Teramura, Y., Tanaka, A. & Jo, T. Effect of coulomb interaction on the X-ray magnetic circular dichroism spin sum rule in 3d transition elements. *J. Phys. Soc. Jpn.* **65**, 1053–1055 (1996).
- Edmonds, K. et al. Ferromagnetic moment and antiferromagnetic coupling in $(\text{Ga}, \text{Mn})\text{As}$ thin films. *Phys. Rev. B* **71**, 064418 (2005).
- Piamonteze, C., Miedema, P. & De Groot, F. M. F. Accuracy of the spin sum rule in XMCD for the transition-metal L edges from manganese to copper. *Phys. Rev. B* **80**, 184410 (2009).
- Smart, J. S. *Effective Field Theories of Magnetism* (W. B. Saunders, Philadelphia, 1966).
- Li, Y., Winter, S. M., Kaib, D. A. S., Riedl, K. & Valenti, R. Modified Curie-Weiss law for j_{eff} magnets. *Phys. Rev. B* **103**, L220408 (2021).
- Dagotto, E., Hotta, T. & Moreo, A. Colossal magnetoresistant materials: the key role of phase separation. *Phys. Rep.* **344**, 1–153 (2001).
- Moulder, J. F., Stickle, W. F., Sobol, P. E. & Bomben, K. D. *Handbook of X-ray Photoelectron Spectroscopy* (Perkin-Elmer Corporation, Eden Prairie, Minnesota, 1992).
- van der Laan, G. & Thole, B. T. Strong magnetic X-ray dichroism in 2p absorption spectra of 3d transition-metal ions. *Phys. Rev. B* **43**, 13401 (1991).
- Ney, A., Kammermeier, T., Ney, V., Ollefs, K. & Ye, S. Limitations of measuring small magnetic signals of samples deposited on a diamagnetic substrate. *J. Magn. Magn. Mat.* **320**, 3341–3346 (2008).
- Buchner, M., Höfler, K., Henne, B., Ney, V. & Ney, A. Tutorial: basic principles, limits of detection, and pitfalls of highly sensitive SQUID magnetometry for nanomagnetism and spintronics. *J. Appl. Phys.* **124**, 161101 (2018).
- Sawicki, M., Stefanowicz, W. & Ney, A. Sensitive SQUID magnetometry for studying nanomagnetism. *Semicond. Sci. Technol.* **26**, 064006 (2011).
- Schlipf, J. et al. Top-down approaches towards single crystal perovskite solar cells. *Sci. Rep.* **8**, 1–8 (2018).
- Saidaminov, M. I. et al. High-quality bulk hybrid perovskite single crystals within minutes by inverse temperature crystallization. *Nat. Commun.* **6**, 7586 (2015).

37. Saliba, M. et al. Cesium-containing triple cation perovskite solar cells: improved stability, reproducibility and high efficiency. *Energy Environ. Sci.* **9**, 1989–1997 (2016).
38. Noll, T. & Radu, F. The mechanics of the VEKMAG experiment. in *Proc. of MEDSI2016, Barcelona, Spain 370–373* (2016).

Acknowledgements

Use of the Helmholtz Innovation Lab HySPRINT and the X-ray Core Lab at Helmholtz-Zentrum Berlin for sample preparation is gratefully acknowledged.

Author contributions

O.R. conceived the project, designed the research, and supervised the project. M.S. fabricated the single crystal samples, prepared the samples for experiments, performed the experimental measurements, performed data analysis, and contributed to the data interpretation. O.R. and M.S. wrote the paper with input from M.K., K.S., and F.R. All authors contributed to discussions, writing, and revising the paper. M.K. performed data analysis and contributed to the data interpretation and discussions. M.A.F. fabricated the film samples and performed XRD measurements. K.S. and M.S. conducted SQUID measurements and analyzed the data. F.R. conducted XAS/XMCD measurements. M.S., F.R. C.L., K.C., and J.M.T. prepared samples for measurements and performed XAS/XMCD experiments.

Funding

Open Access funding enabled and organized by Projekt DEAL.

Competing interests

The authors declare no competing interests.

Additional information

Supplementary information The online version contains supplementary material available at <https://doi.org/10.1038/s42005-023-01178-0>.

Correspondence and requests for materials should be addressed to Oliver Rader.

Peer review information *Communications Physics* thanks Ki-Yeon Kim and the other anonymous reviewer(s) for their contribution to the peer review of this work.

Reprints and permission information is available at <http://www.nature.com/reprints>

Publisher's note Springer Nature remains neutral with regard to jurisdictional claims in published maps and institutional affiliations.



Open Access This article is licensed under a Creative Commons Attribution 4.0 International License, which permits use, sharing, adaptation, distribution and reproduction in any medium or format, as long as you give appropriate credit to the original author(s) and the source, provide a link to the Creative Commons license, and indicate if changes were made. The images or other third party material in this article are included in the article's Creative Commons license, unless indicated otherwise in a credit line to the material. If material is not included in the article's Creative Commons license and your intended use is not permitted by statutory regulation or exceeds the permitted use, you will need to obtain permission directly from the copyright holder. To view a copy of this license, visit <http://creativecommons.org/licenses/by/4.0/>.

© The Author(s) 2023